Accounting for Circumferential Flow Nonuniformity in a Multistage Axial Compressor

Fangyuan Lou[1]
School of Mechanical Engineering,
Purdue University,
West Lafayette, IN 10084
e-mail: loufy@tsinghua.edu.cn

Douglas R. Matthews
School of Mechanical Engineering,
Purdue University,
West Lafayette, IN 47907
e-mail: matthe18@purdue.edu

Nicholas J. Kormanik III
School of Mechanical Engineering,
Purdue University,
West Lafayette, IN 47907
e-mail: nkormani@purdue.edu

Nicole L. Key
School of Mechanical Engineering,
Purdue University,
West Lafayette, IN 47907
e-mail: nkey@purdue.edu

The flow field in a compressor is circumferentially nonuniform due to geometric imperfections, inlet flow nonuniformities, and blade row interactions. Therefore, the flow field, as represented by measurements from discrete stationary instrumentation, can be skewed and contributes to uncertainties in both calculated one-dimensional performance parameters and aerodynamic forcing functions needed for aeromechanics analyses. Considering this challenge, this article documents a continued effort to account for compressor circumferential flow nonuniformities based on discrete, undersampled measurements. First, the total pressure field downstream of the first two stators in a three-stage axial compressor was measured across half of the annulus. The circumferential nonuniformities in the stator exit flow, including vane wake variability, were characterized. In addition, the influence of wake variation on stage performance calculations and aerodynamic forcing functions were investigated. In the present study for the compressor with an approximate pressure ratio of 1.3 at the design point, the circumferential nonuniformity in total pressure yields an approximate 2.4-point variation in isentropic efficiency and 54% variation in spectral magnitudes of the fundamental forcing frequency for the embedded stage. Furthermore, the stator exit circumferential flow nonuniformity is accounted for by reconstructing the full-annulus flow using a novel multiwavelet approximation method. Strong agreement was achieved between experiment and the reconstructed total pressure field from a small segment of measurements representing 20% coverage of the annulus. The analysis shows the wake–wake interactions from the upstream vane rows dominate the circumferentially nonuniform distributions in the total pressure field downstream of stators. The features associated with wake–wake interactions accounting for passage-to-passage variations are resolved in the reconstructed total pressure profile, yielding representative mean flow properties and aerodynamic forcing functions.
[DOI: 10.1115/1.4056933]

Keywords: circumferentially nonuniform flow, flow reconstruction, multiwavelet approximation, multistage axial compressor, compressed sensing, experimental method

1 Introduction

Circumferential nonuniformities in a compressor flow field exist due to geometric imperfections (manufacturing inconsistencies, eccentricities, erosion and wear, etc.), inlet flow nonuniformities, wakes from upstream stator row(s), the potential field from both upstream and downstream stator rows, as well as their aerodynamic interactions. The influences of the circumferential flow nonuniformity are twofold. First, it can introduce instrumentation error, further contributing to uncertainties in calculating one-dimensional performance metrics during rig or engine tests with rakes at fixed locations. Second, the nonuniformities create challenges in characterizing the aerodynamic blade forcing function for forced response because of the passage–passage variations caused by blade row interactions, essentially contributing an aerodynamic mistuning to the wake forcing function.

In engine or rig tests, the one-dimensional performance metrics are determined based on the measurements from rakes placed at several stations around the annulus at fixed axial positions [1]. In a state-of-the-art measurement procedure, probes are typically placed behind different blades at different relative pitchwise positions to capture the free flow and the wake flow separately, with the assumption of the periodic flow from passage to passage. The measurements are then pitchwise averaged to yield a representative mean flow property. However, for blade rows with dissimilar vane counts that result in "aperiodic" flow among passages around the annulus [2], the data acquired at discrete locations around the annulus can be skewed and contribute to the uncertainty, or so-called instrumentation error, in the reduced one-dimensional performance metrics. For instance, He et al. [3] conducted a full-annulus unsteady Reynolds-averaged Navier–Stokes (URANS) simulation in a 3.5-stage axial compressor at midspan and showed that the circumferentially nonuniform flow can cause more than a one-point error in compressor stage performance measurements. Later, Methel et al. [4] experimentally characterized the stator wake variability in a three-stage axial compressor through a rigorous traverse of different vane passages. Results showed three points in variation in overall compressor efficiency and up to 15 points variation for individual stage efficiency based on pressure and temperature variations observed among passages. More recently, Chilla et al. [5] investigated the instrumentation errors caused by circumferential flow variations in an eight-stage axial compressor representative of a small core compressor of an aero-engine. The analysis showed that a baseline probe configuration with three equally spaced probes around the annulus yields a maximum of 0.8% error in flow capacity and 2.8 points error in compressor isentropic efficiency. As compressor designers are leveraging design choices that result in efficiency improvements on the order of 0.1 points, a 2.8-point uncertainty in efficiency due to instrumentation error makes it difficult to assess the

[1]Corresponding author.

Contributed by the International Gas Turbine Institute (IGTI) of ASME for publication in the Journal of Turbomachinery. Manuscript received July 14, 2021; final manuscript received October 25, 2022; published online March 6, 2023. Tech. Editor: David G. Bogard.

performance improvements in technology development programs. Therefore, the effects of the circumferential flow nonuniformity must be accounted for in both design of experiment and data reduction.

In addition to one-dimensional performance metrics, the prediction of aerodynamic blade forcing functions in forced response vibratory conditions is an especially important topic in turbomachinery design as it drives rotor resonant vibratory response. However, in contrast to the enhanced capability achieved for mistuned forced response prediction [6,7], the influence of circumferential flow nonuniformity on aerodynamic excitation is less understood. The wake from the upstream blade row and the potential field from the downstream blade row are considered the main causes for excitation, and the aerodynamic excitation reduced from steady single-passage computational fluid dynamics (CFD) simulations [6,8] is typically used to predict the rotor resonant response. However, the results from Methel et al. showed more than 60% variations in spectral magnitudes of the fundamental forcing frequency due to stator wake variability among investigated passages [4]. In a recent study, Schoenenborn [9] suggested that the aerodynamic excitation can change significantly from blade to blade due to the superposition of the Tyler–Sofrin (or scattered or spinning) modes, which refer to the acoustic interaction with blade rows further upstream or downstream and may have a significant impact on blade forcing.

2 Scope of the Article

While it is important to account for circumferential flow nonuniformity, there is very limited experimental coverage on this topic. The primary reason is the scarcity of multistage compressor facilities with detailed circumferential flow field traversing capability. Even when a facility has the capability to traverse a probe circumferentially, it is still a challenging task to perform a full-annulus traverse to capture the circumferential flow nonuniformity. To the authors' best knowledge, the only study in the open literature with a focus on experimental characterization of the stator wakes and their variability was conducted by Methel et al. [4] in a three-stage axial compressor. A minimum of 6 wakes and a maximum of 12 wakes were measured at the exit of each vane row by simultaneously indexing all vane rows along the circumferential direction. Amid the inspiring observations, it is worth noting that the compressor configuration utilized had the same vane count for the inlet guide vane (IGV), stator 1 (S1), and stator 2 (S2), and thus, the blade row interactions were less representative of the conditions in real engines with dissimilar vane counts. In the present study, a different compressor configuration with the reduced vane count of S1 was utilized to provide a more suitable multirow environment.

The objective of this article is to account for compressor circumferential flow nonuniformity through a two-step effort:

(1) Characterize the circumferential flow nonuniformity including stator wake variability.
(2) Resolve the flow features accounting for circumferential flow nonuniformity.

Correspondingly, the article is organized in the following manner. First, about half of the annulus total pressure field downstream of the first two stators in a three-stage axial compressor was measured through rigorous circumferential traverses by indexing all vane blade rows simultaneously with respect to the stationary total pressure rakes. The circumferential nonuniformities in the stator exit flow were analyzed, and the resulting influence on stage efficiency and wake forcing functions were characterized. Furthermore, the stator exit circumferential flow nonuniformity is accounted for by reconstructing the full-annulus flow using a novel multiwavelet approximation method. The method's fidelity is examined by comparing the reconstructed signal with experimental results in both spectral and spatial domains. The roles of blade row interactions in stator exit circumferential flow nonuniformity are discussed.

3 Experimental Approach

The experiment was conducted in the Purdue 3-Stage (P3S) Axial Compressor Research Facility using the PAX100 compressor with a reduced vane count for stator 1 (denoted PAX101). Though not detailed here, thorough documentation of the research facility can be found in Ref. [10], where details about inlet flow conditioning to ensure no inlet distortions are delivered to the test section are presented. The PAX100 compressor design features an IGV followed by three stages, shown in Fig. 1. All three of the rotors are integrally bladed, and each stator row is uniquely manufactured as a 180-deg segment featuring shrouded vanes. During operation, each stator row also can circumferentially traverse an angular distance up to approximately 15 deg, or more than two stator vane passages. This allows for stationary rakes to characterize vane passage profiles in detail along the pitchwise direction.

In the original PAX100 configuration, the IGV, stator 1 (S1), and stator 2 (S2) all have the same vane count of 44 providing a unique environment to study the effects of vane clocking on compressor aerodynamic performance. The added benefit of only needing to characterize one passage to effectively characterize the entire annulus of the compressor (neglecting the effects of S3) was an advantage in acquiring accurate performance measurements. This unique configuration is excellent for research, but it is not a typical luxury for compressors in real engines, in which the stators typically have dissimilar vane counts. In addition, the same vane count of S1 and S2 makes their relative impact on rotor 2 (R2) resonant response indistinguishable using the PAX100 configuration. To solve the problem, a reduced-count S1 vane row was designed by Monk [11], featuring 38 vanes instead of 44 (19 vanes per 180-deg segment). With the introduction of a different, reduced vane count for S1 into the standard compressor configuration, the periodic boundary condition is no longer applicable for an individual passage. In other words, the full-annulus could not be approximated by a single-vane passage traverse. Therefore, the characterization of representative passage profiles for the PAX101 configuration gets more complicated.

To shed light on this topic, a comprehensive experimental campaign was conducted following a complex vane traverse scheme developed by Kormanik [12]. The test campaign was conducted at 86% corrected speed on the design speed peak efficiency loading line, shown in Fig. 2. This part-speed operation was selected to characterize the forcing functions for R2 forced response near the resonant crossing of the 38EO excitation of the R2 first torsion vibratory mode. In the experiment, seven-element total pressure rakes were placed behind S1, R2, and S2 at three different

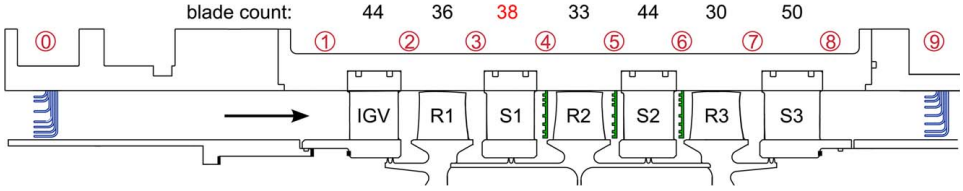

Fig. 1 Reduced S1 vane count configuration of PAX101

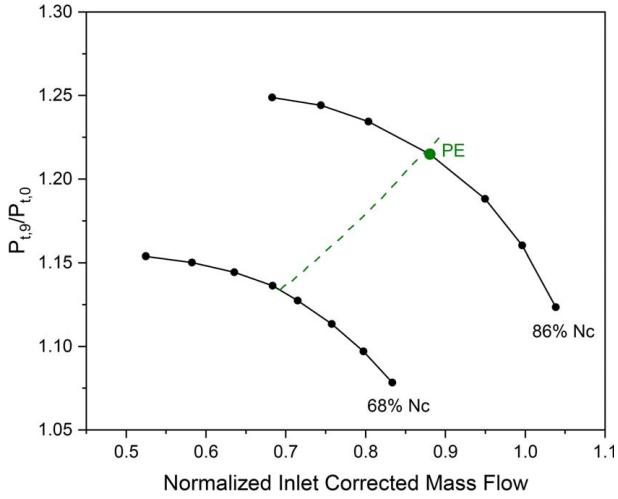

Fig. 2 Compressor normalized total–total pressure map

circumferential locations (noted as location A, B, and D, respectively, in Fig. 3). The rake port axial locations for S1, R2, and S2 are at stations 4, 5, and 6, respectively, from Fig. 1. The rakes have Kiel head probes at 12%, 20%, 35%, 50%, 65/70%, 80%, and 88% span. In each traverse, all vane rows were moved together over an entire S1 vane pitch at a step of every 5% of the S1 vane passage. The position of each vane row is measured using the feedback control with precision string potentiometers having a repeatability of 0.1% of the vane passage. The pressure transducers were zeroed every 20 min during compressor operation to minimize the effects of thermal drift. The mechanical speed was constantly adjusted to maintain the corrected speed within ±0.1% of the target corrected speed. The ambient reference pressure was measured using a high accuracy barometric transducer with ±0.073% full-scale accuracy. In combination with the measured gage pressures, the largest uncertainty on individual stage total pressure ratio is less than 2×10^{-4} [4]. At the end of the test campaign, a total of seven traverses were performed, covering approximately 58.6 deg of effective travel around the annulus for each rake or 16.3% of the entire annulus. With the implementation of stationary rakes at three measurement locations (A, B, and D), this delivers a mapping of 19 and 22 passages for S1 and S2, respectively, indicated by the shaded areas in Fig. 3.

4 Characterization of Circumferential Flow Nonuniformity and Its Effects

In a multistage compressor with different vane counts, wake–wake interactions and wake–potential field interactions occur due to different circumferential positions of wakes from upstream rows and potential field effects from downstream rows. This

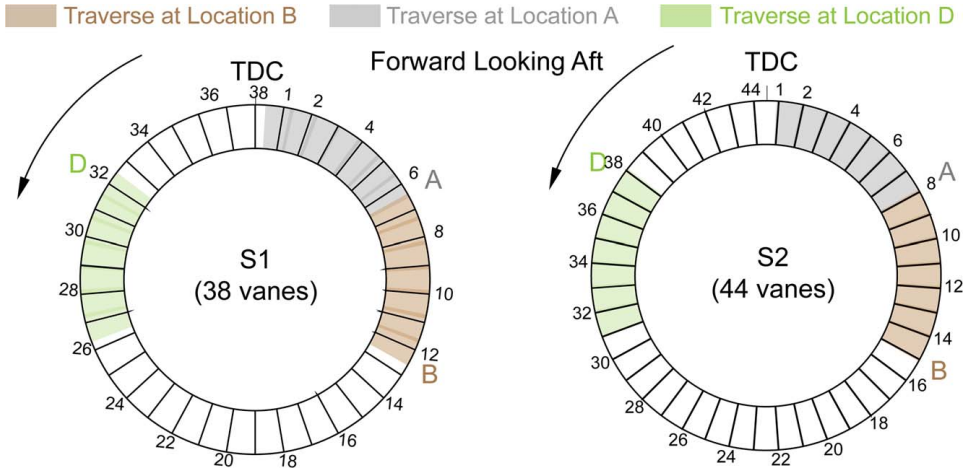

Fig. 3 Measurement locations for the traverses downstream of stator 1 and stator 2

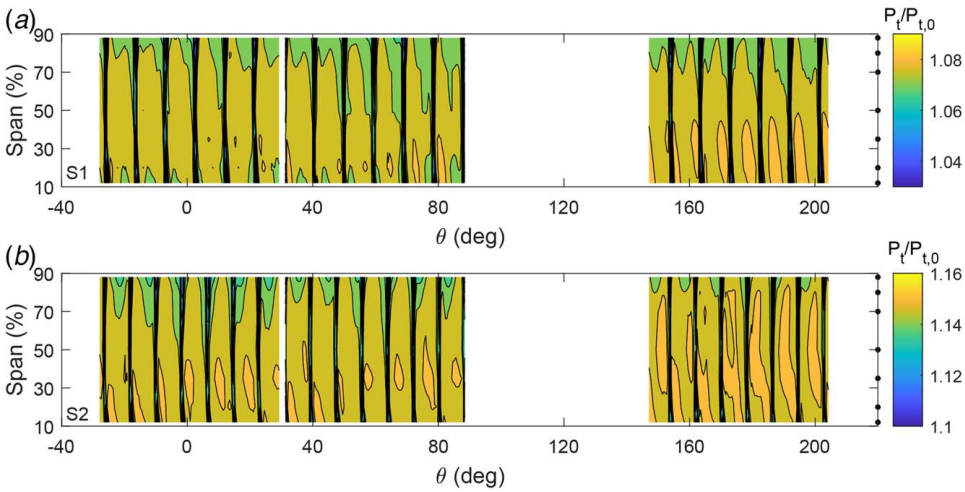

Fig. 4 Normalized total pressure contours downstream of (*a*) stator 1 and (*b*) stator 2 from experiment

superposition of wakes and potential field, with different periodicity, results in nonuniform flow distributions around the annulus.

4.1 Passage–Passage Variation and Its Effects on Stage Isentropic Efficiency Evaluation. Figure 4 shows the normalized measured total pressure contour at S1 exit (Fig. 4(*a*)) and S2 exit (Fig. 4(*b*)). The total pressure is normalized by the area-averaged total pressure at the compressor inlet, and the solid symbols indicate the spanwise probe locations. There are significant passage-to-passage variations in the total pressure field downstream of both S1 and S2. Aside from these variations, there is a repetitive pattern in terms of the size and shape for the low-momentum flow at the suction surface near the shroud, cycling approximately once every 60 deg. Though there are many contributing factors to the observed passage-to-passage variations, such as geometric imperfections, the dominant contributor is the blade row interactions including wake–wake interactions and wake–potential field interactions. The analysis of each contribution will be presented in the following section.

Two important takeaways can be drawn based on the observed substantial passage-to-passage variations. On the one hand, as compressor design heavily relies on computational tools and uses CFD methods for steady flow simulations of isolated blade rows utilizing periodic boundary conditions, the results from these simulations can be biased in representing the real flow field in the compressor. On the other hand, measurements from discrete stationary instrumentation can also skew measurements of the dedicated flow field. Both can contribute to disagreements between simulations and experiments.

For instance, Fig. 6 shows variations in the calculated stage isentropic efficiency due to circumferential flow nonuniformity. In the analysis, the stage isentropic efficiency is evaluated using the definition:

$$\eta = \frac{h_{t,\text{exit},s} - h_{t,\text{inlet}}}{h_{t,\text{exit}} - h_{t,\text{inlet}}} \tag{1}$$

as a function of stagnation enthalpies. The stagnation enthalpies along with other thermodynamic properties are retrieved from the National Institute of Standards and Technology reference fluid thermodynamic and transport properties database, REFPROP [13]. Considering efficiency calculations based on total pressure and total temperature measurements at stage inlet and exit, a previous study shows that it is inherently difficult to accurately measure the isentropic efficiency for compressors or stages with smaller total pressure ratios, primarily associated with the total temperature measurement uncertainties at the compressor or stage inlet [14]. For instance, the uncertainty in efficiency for a low-pressure ratio compressor can be greater than 5 points [14].

However, the variations in stage efficiency calculations presented in Fig. 5 only account for variations in stator exit total pressure among passages, while the inlet total pressure, total temperature, and exit total temperature are kept constant. Each symbol in Fig. 5 represents the calculated stage efficiency based on the pitchwise averaged total pressure across one passage. The passage-to-passage variations in stator exit total pressure result in an approximate 2.3-point variation in efficiency for the first stage and a 2.4-point variation in efficiency for the embedded (second) stage. Furthermore, this is a significant variation in the calculated stage efficiency, even using measurements from the same rakes. For instance, there is an approximate 0.7-point variation in the calculated stage 1 efficiency using measurements at port A, and measurements from ports B and C give a 1.3-point variation. Similarly, the variations in stage 2 efficiency are 0.8 points for locations A and C and 0.7 points for location B.

A common approach adopted to reconcile the effects of passage-to-passage variation is to use the average profiles from several passages. As shown in Fig. 6, this approach does reduce the variations in the calculated stage efficiency to a certain extent. For instance, the variation in the calculated efficiency for the first

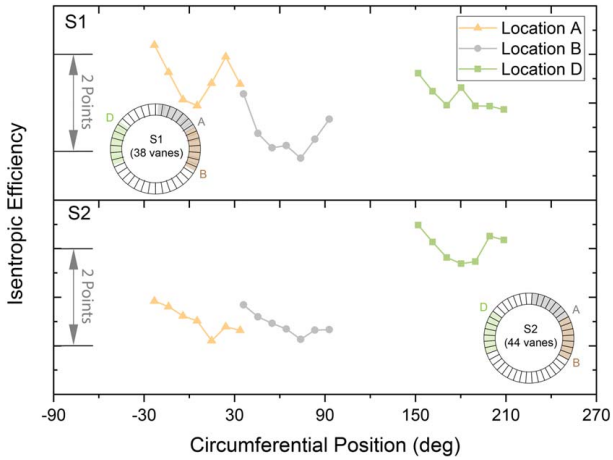

Fig. 5 Effects of circumferential flow nonuniformity on stage efficiency characterization using single-passage pitchwise averaged profiles

stage is reduced to 1.9 points by using the average passage profile from 3 passages, and this value is further reduced to 1.3 points and 0.9 points when using average profiles from 7 and 11 passages, respectively. Similarly, the variations in the calculated efficiency for the second stage is reduced to 2.1 points, 1.8 points, and 1.2 points when using average profiles from 3, 7, and 11 passages, respectively. However, the progress achieved in reducing variations in the calculated efficiency using this approach is quite incremental.

Lastly, it is important to note that the variations in the calculated stage efficiency presented in Figs. 5 and 6 only account for variations in stage exit total pressure. Research has shown that the calculated efficiency is more sensitive to variations in total temperature [14]. Therefore, the variations in stage efficiency can be significant, up to 15 points variation in the calculated stage efficiency at peak efficiency condition [4].

4.2 Effects in Predicting Aerodynamic Forcing Function. To date, the prediction of aerodynamic blade forcing remains a very important topic in making an aeroelastic assessment of blade resonant response. Aerodynamic excitation can arise due to wakes from upstream vane rows or struts, the potential field of both upstream and downstream vane rows, as well as their aerodynamic interactions. Stator wakes are typically considered the primary contributor to aerodynamic excitation for the downstream rotor. The strength of the aerodynamic forcing function on the rotor due to the stator wakes can be quantified with a Fourier analysis, where the spatial Fourier transform (FT) of the stator exit flow field is

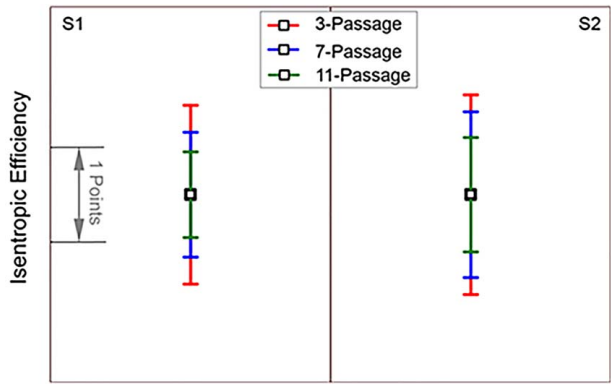

Fig. 6 Effects of circumferential flow nonuniformity on stage efficiency characterization using multipassage averaged profiles

computed. Ideally, information of the full-annulus stator exit flow is required to conduct a spatial Fourier transform. However, this requires expanding the computational domain to the whole annulus and results in a significant increase in the computational cost. In practical applications, results from single-passage steady CFD simulations, or a rake traverse across a single passage, are typically used to predict the aerodynamic forcing function. The spatial Fourier transform was conducted by repeating the single-passage profile identically to the appropriate number of vanes per row, assuming a periodic boundary condition among passages. Though this is cost effective and simple to implement, forcing a repetitive pattern equal to the blade row's vane count acts as a spatial bandpass filter that removes all frequencies not related to the blade row vane counts.

In the compressor used for the present study, the main aerodynamic forcing functions for the embedded rotor (rotor 2) and rotor 3 are the wakes shed from the upstream stators, namely, stator 1 and stator 2, and thus are the main focus of the present section. The results at 88% span, nearest to the shroud, are presented since the largest deflection for the first torsion vibratory mode occurs at the tip of the rotor blade.

Figures 7(*a*) and 8(*a*) show all indexed passage profiles measured at 88% span downstream of stator 1 and stator 2, respectively. To isolate the variations related to the instrumentation, the profiles acquired using different rakes are shown separately. There are evident variations in the total pressure profiles at all three measurement locations. In addition to the variations in wake width and depths, which have been investigated thoroughly in Ref. 4, there are also variations in the primary flow profiles. These primary flow profile variations are primarily attributed to the superposition of wakes shed from upstream blade rows and a circumferentially varying clocking effect associated with the different vane counts of the upstream vane rows. For instance, at certain circumferential locations downstream of stator 2, the wakes of stator 2 are superimposed on the upstream stator 1 wakes. This occurs at different pitchwise positions around the annulus due to the different S1 and S2 vane counts. As a result, at one pitch position behind different blades of stator 2, a different total pressure is observed. Though similar phenomena have been reported in several numerical studies (i.e., the study conducted by Stummann et al.), to the best knowledge of authors, this is the first time that experimental results document this phenomenon. In addition, when comparing to profiles downstream of S1, these wake–wake interactions get intensified in the embedded stage, resulting in larger variations and a broader envelope for the total pressure profiles downstream of stator 2.

Figures 7(*b*) and 8(*b*) show the variations in the calculated aerodynamic excitation due to the passage-to-passage total pressure

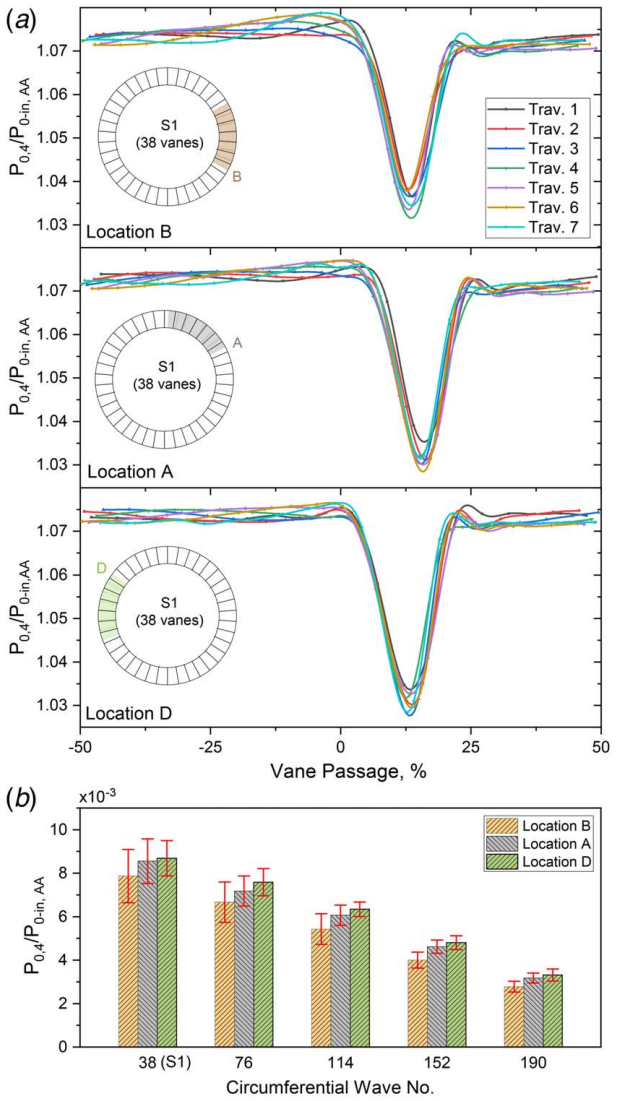

Fig. 7 Stator 1 downstream (*a*) passage–passage total pressure profile variability and (*b*) forcing function variability at 88% span

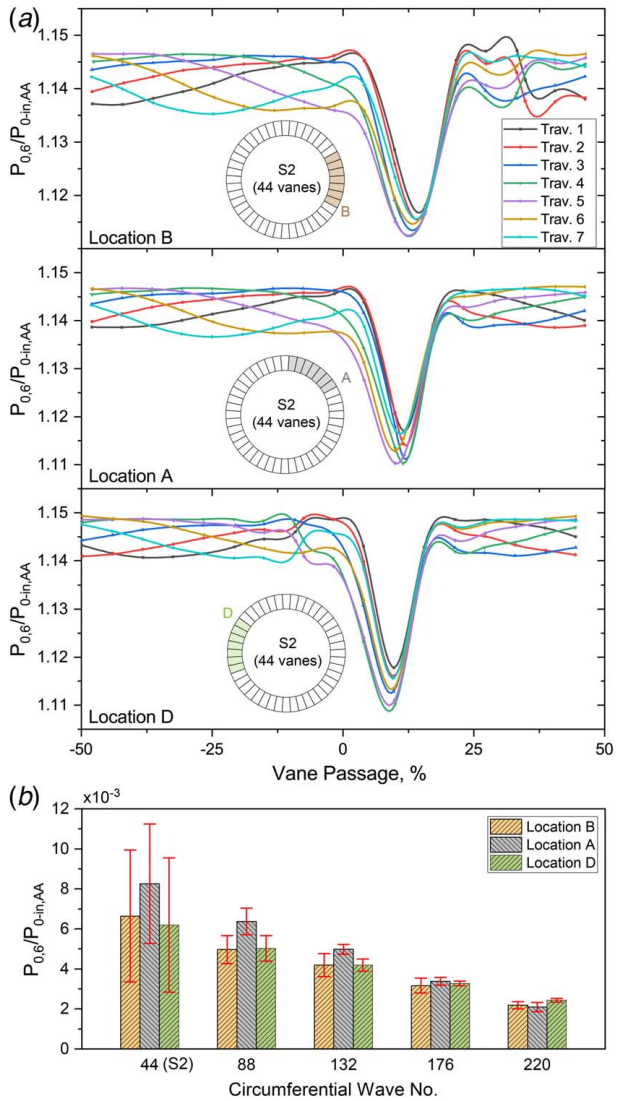

Fig. 8 Stator 2 downstream (*a*) passage–passage total pressure profile variability and (*b*) forcing function variability at 88% span

profile variability. The aerodynamic excitation variability, indicated by the error bar, is the standard deviation of the forcing functions based on different indexed single-passage total pressure profiles. For the forcing functions arising from S1 wakes, there is a 9.3% variability in the magnitude of the excitation for the fundamental harmonic and an 8.2% variability for the second harmonic. Also, the variations observed at different measurement locations are of similar magnitude. For instance, the magnitudes variations for the first harmonic from measurements at locations B, A, and D are 9.3%, 12.0%, and 15.6%, respectively. In addition, when comparing to the S1 wake forcing functions, there is more substantial variability in the S2 wake forcing functions, shown in Fig. 8(*b*). For instance, there is 54% variability in the excitation magnitude for the fundamental harmonic and 36% variability for the second harmonic of S2 wakes.

When using results from a single-passage simulation or traverse, these passage-to-passage variations in the total pressure can result in more than two points variation in the calculated stage efficiency and up to 54% variation in the magnitudes for the fundamental harmonic of the forcing function. The variations in calculated stage isentropic efficiency as well as aerodynamic excitations due to the passage-to-passage flow variability (as shown in Figs. 5, 7, and 8) illustrate the limitations of using a single-passage profile as representative of the full-annulus flow. Therefore, it is important to account for the effects of the circumferential flow nonuniformity in experimental design, simulation setup, and data analysis.

5 Accounting for the Circumferential Flow Nonuniformity

To understand the features associated with circumferential flow nonuniformity, the total pressure profiles acquired at midspan downstream of stator 1 and stator 2 are plotted in terms of their global circumferential position, as shown in Fig. 9. Measurements from different rake locations are labeled in the figure. At each rake location, the index of traverses from one to seven is also labeled in the figure. First, as expected, the total pressure profile downstream of the stators is dominated by the wakes shed from the immediate upstream vane row. For instance, the total pressure profile downstream of S1 is dominated by the S1 wakes with a

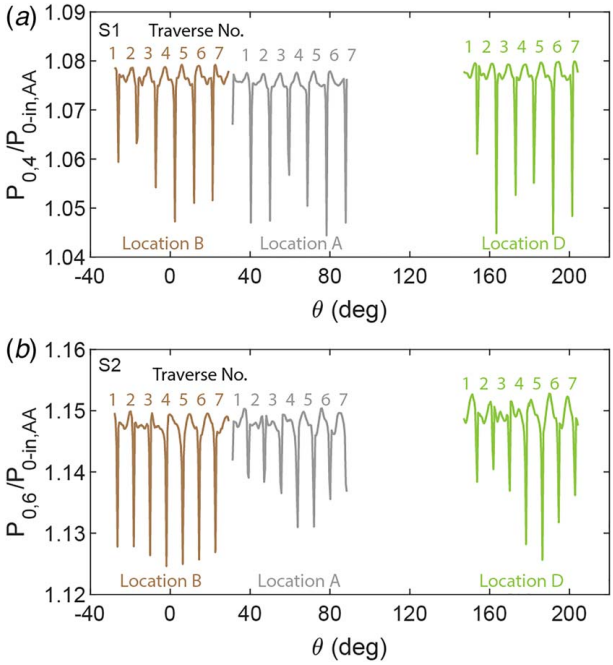

Fig. 9 Normalized total pressure measured at 50% span downstream of (*a*) stator 1 and (*b*) stator 2

fundamental harmonic of 38 (S1 vane count) corresponding to the observed 19 wakes over an approximate half annulus, Fig. 9(*a*). Similarly, the total pressure profile downstream of S2 is dominated by the S2 wakes with a fundamental harmonic of 44 (S2 vane count) in correspondence with the observed 22 wakes over an approximate half annulus, Fig. 9(*b*). Second, the stator–stator interactions result in complicated patterns in the total pressure profiles.

There are three categories of stator–stator interactions:

(1) Superposition of wakes from upstream vane rows.
(2) Effects of the potential field from both upstream and downstream vane rows.
(3) Effects of different levels of wake–wake interactions around the annulus.

In this section, the contribution of each category to the circumferential flow nonuniformity is examined. Then, the features determining the circumferentially nonuniform flow are included in the multiwavelet approximation method to account for the circumferential nonuniformity.

5.1 Reconstruction of the Circumferential Nonuniform Flow Using a Multiwavelet Approximation Method. In theory, the circumferential flow field in turbomachines with a spatial periodicity of 2π can be described in terms of infinite serial wavelets of different wavenumbers:

$$x(\theta) = c_0 + \sum_{i=1}^{\infty} (\mathrm{A}_i \sin(W_{n,i}\theta + \varphi_i)) \tag{2}$$

wherein $x(\theta)$ represents the flow property along the circumferential direction, c_0 represents the DC component of the signal, W_n represents wavenumber, variables A and φ represent the magnitude and phase of the wavelet, and subscript i indicates the properties associated with the $i$thwavenumber. Furthermore, defining $\mathrm{a}_i = \mathrm{A}_i \cos \varphi_i$ and $\mathrm{b}_i = \mathrm{A}_i \sin \varphi_i$, Eq. (2) can be described as follows:

$$x(\theta) = c_0 + \sum_{i=1}^{\infty} (\mathrm{a}_i \sin(W_{n,i}\theta) + \mathrm{b}_i \cos(W_{n,i}\theta)) \tag{3}$$

However, with infinite unknowns in Eqs. (2) and (3), no solution can be found to these equations.

Recent studies show that multistage compressor flow fields are typically dominated by several wavenumbers, motivating a novel multiwavelet approximation method for reconstruction of the circumferential nonuniform flow in turbomachines. Details of the method can be found in Ref. [15]. The fundamental concept of the method is to approximate the circumferential variations of the flow field in turbomachines using a few (N) dominant wavelets instead of an infinite number of wavelets:

$$x(\theta) \approx c_0 + \sum_{j=1}^{N} (\mathrm{a}_j \sin(W_{n,j}\theta) + \mathrm{b}_j \cos(W_{n,j}\theta)) \tag{4}$$

To solve for the information for the N dominant wavelets in Eq. (4), a minimum of $2N+1$ data points measured at different circumferential locations, $\boldsymbol{\theta} = (\theta_1, \theta_2, \theta_3, \ldots \theta_m)$, is required. In practical applications, Eq. (4) is typically cast in a matrix form:

$$\boldsymbol{AF} = \boldsymbol{x} \tag{5}$$

where $\boldsymbol{A}$ is known as the design matrix and is a function of wavelets W_n and the circumferential positions of the measurements θ. The vector $\boldsymbol{F}$ contains all unknown coefficients, and $\boldsymbol{x}$ is the vector with all measurements acquired at different circumferential locations. The mathematical expressions for $\boldsymbol{A}$, $\boldsymbol{F}$,

and $\boldsymbol{x}$ are as follows:

$$\boldsymbol{A}=\begin{pmatrix} \sin W_{n,1}\theta_1 & \cos W_{n,1}\theta_1 & \cdots & \sin W_{n,N}\theta_1 & \cos W_{n,N}\theta_1 & 1 \\ \sin W_{n,1}\theta_2 & \cos W_{n,1}\theta_2 & \cdots & \sin W_{n,N}\theta_2 & \cos W_{n,N}\theta_2 & 1 \\ \vdots & \vdots & \vdots & \vdots & \vdots & \vdots \\ \sin W_{n,1}\theta_m & \cos W_{n,1}\theta_m & \cdots & \sin W_{n,N}\theta_m & \cos W_{n,N}\theta_m & 1 \end{pmatrix}$$

$$\boldsymbol{F}=\begin{pmatrix} a_1 \\ b_1 \\ \vdots \\ a_N \\ b_N \\ c_0 \end{pmatrix}$$

$$\boldsymbol{x}=\begin{pmatrix} x(\theta_1) \\ x(\theta_2) \\ \vdots \\ x(\theta_m) \end{pmatrix}$$

The unknown vector can be obtained from a direct inverse matrix operation $\boldsymbol{F}=\boldsymbol{A}^{-1}$ for a balanced system or a least-square-fitting method for an over-determined system.

Two considerations are important when reconstructing the circumferentially nonuniform flow field using the multiwavelet approximation method. The first is the condition number of the linear system described in Eq. (5), and the second is the confidence in the reconstructed signal. The condition number of the design matrix $\boldsymbol{A}$ measures how sensitive the reconstructed signal $\boldsymbol{F}$ responds to errors in the measurements $\boldsymbol{x}$ with a smaller number, indicating a "well-conditioned" system. The condition number is calculated using the formula:

$$k=\|\boldsymbol{A}\|\|\boldsymbol{A}^{+}\| \tag{6}$$

where $\boldsymbol{A}^{+}$ is the inverse of matrix $\boldsymbol{A}$ for a square matrix and the Moore–Penrose pseudoinverse of matrix $\boldsymbol{A}$ for a rectangular matrix.

To evaluate the confidence in the reconstructed signal, the Pearson correlation coefficient or Pearson's r is utilized, and it is calculated as follows:

$$\rho=\frac{\sum_{j=1}^{m}x_j x_{fit,j}-\left(\sum_{j=1}^{m}x_j\sum_{j=1}^{m}x_{fit,j}\right)/m}{\sqrt{\left(\sum_{j=1}^{m}x_j^2-\left(\sum_{j=1}^{m}x_j\right)^2/m\right)\left(\sum_{j=1}^{m}x_{fit,j}^2-\left(\sum_{j=1}^{m}x_{fit,j}\right)^2/m\right)}}, \tag{7}$$

where $x(\theta)$ is the true signal from measurements and $x_{fit}(\theta)$ represents the reconstructed signal. The range for Pearson's r is between 0 and 1. For a well-reconstructed circumferential flow field, the predicted flow properties should align with actual values at all the measurement locations and yield a value of nearly 1 for the Pearson's r, and vice versa.

Two questions arise regarding the effectiveness of the multiwavelet approximation method:

(1) How well does it characterize the flow features in the spectral domain?
(2) How well does the reconstructed flow represent the true flow field in the spatial domain?

5.2 Comparison of the Forcing Function Predicted Using the Multiwavelet Approximation Method With Results From Spatial Fourier Transform. To evaluate the multiwavelet approximation method's accuracy in the spectral domain, the forcing functions associated with the stator 1 and stator 2 downstream total pressure profiles were analyzed using both the multiwavelet approximation method and the spatial Fourier transform method. In both cases, a random single-passage total pressure profile, shown in Fig. 10, was used for the analysis. The spectral magnitudes for the first 12 harmonics were computed. As shown in their respective figures, the multiwavelet approximation method yields almost identical spectral magnitudes to the values predicted by a spatial Fourier transform for all computed harmonics. The maximum deviations between the two methods in the predicted stator 1 and stator 2 associated forcing function for the first six harmonics are less than 5.0%, and 6.0%, respectively. Thus, it suggests the multiwavelet approximation method can predict aerodynamic forcing functions with high fidelity.

A significant advantage associated with the multiwavelet approximation method is that it requires a much smaller data size. As discussed in Sec. 5.1, the characterization of N dominant wavelets requires a data size greater than $2N+1$. Unlike the spatial Fourier transform analysis, where the sampling frequency determines the highest wavenumber, the individual wavelet of any wavenumber

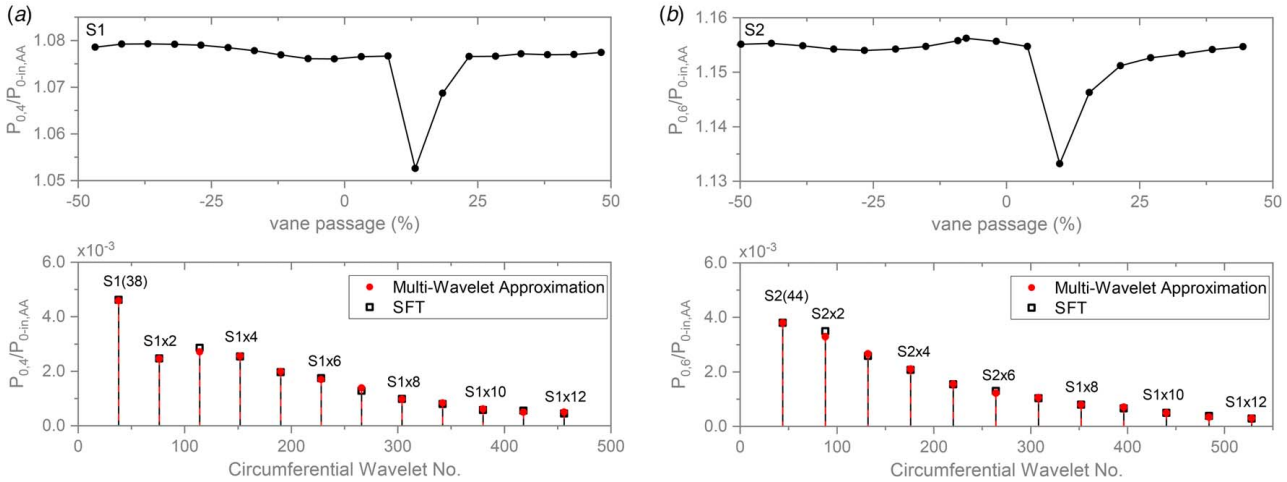

Fig. 10 Comparison of spectral magnitudes calculated from discrete Fourier transform and multiwavelet approximation method for (*a*) stator 1 and (*b*) stator 2 profiles

can be determined from two data points using the multiwavelet approximation method. However, it is worth noting that the multiwavelet approximation method requires pre-knowledge of the dominant wavelets in the flow field.

5.3 Identification of the Dominant Mechanism That Defines the Circumferential Flow Nonuniformity. Before reconstructing the stator exit total pressure field in the spatial domain, information of the dominant mechanism defining the circumferential flow nonuniformity and the appropriate selection of the wavelets are required. For the total pressure downstream of stator 1, the wavelets include the following:

(1) Stator 1 wake, with wavenumbers of 38 and its harmonics;
(2) IGV wake, with wavenumbers of 44 and its harmonics;
(3) Stator 2 potential field, with wavenumbers of 44 and its harmonics;
(4) Stator 3 potential field, with wavenumbers of 50 and its harmonics;
(5) Vane clocking effects, with wavenumbers of 6 (IGV-S1) and its harmonics.

In a similar manner, the total pressure downstream of stator 2 contains wavelets capturing the:

(1) Stator 2 wake, with wavenumbers of 44 and its harmonics;
(2) Stator 1 wake, with wavenumbers of 38 and its harmonics;
(3) IGV wake, with wavenumbers of 44 and its harmonics;
(4) Stator 3 potential field, with wavenumbers of 50 and its harmonics;
(5) Vane clocking effects, with wavenumbers of 6 (S2-S1) and its harmonics.

With the complete information on the wavelets in place, identification of the dominant mechanism, as well as the selection of the appropriate number of wavelets, was achieved through a two-step effort:

(1) The signal was reconstructed using fundamental wavelets related to the experiment. The confidence in the reconstructed signal using Pearson's r was evaluated, where the rank of Pearson's r represents the importance of the mechanism related to the wavelet.
(2) The signal was reconstructed with incremental additions of wavelets of higher harmonics, and the change in the confidence of the reconstructed signal was compared to the original reconstruction. A plateau in the confidence of the reconstructed signal indicates an adequate number of harmonics for that wavelet family.

Figure 11 shows the results obtained by following the aforementioned procedure. As expected, the wakes from S1 (38) and S2 (44) dominate the stator row downstream total pressure field and provides the highest confidence in the reconstructed signal. The effects from the IGV wake (44) and the potential field of S2 (44) cannot be distinguished because of their similar vane counts. However, the results from S2 show that the second dominant effect is the wake shed from upstream S1 (38) instead of the potential field effects of downstream S3 (50). In both cases, the influence of the S1–S2 interaction (6) on the circumferential nonuniformity is minor. Additionally, the potential field of the downstream stator decays very quickly and contributes very little to circumferential flow nonuniformity. Lastly, the increase in Pearson's r at higher harmonics associated with 6/rev and downstream stator potential field effects are caused by signal aliasing at higher wavelet numbers.

The appropriate number of harmonics needed for flow reconstruction can also be derived from the results in Fig. 11. Using the total pressure field downstream of S2 as an example, the confidence in the reconstructed signal starts to plateau after the inclusion of the first eight harmonics for S2 wake, and thus, it suggests a minimum of eight wavelets needed for the S2 wake.

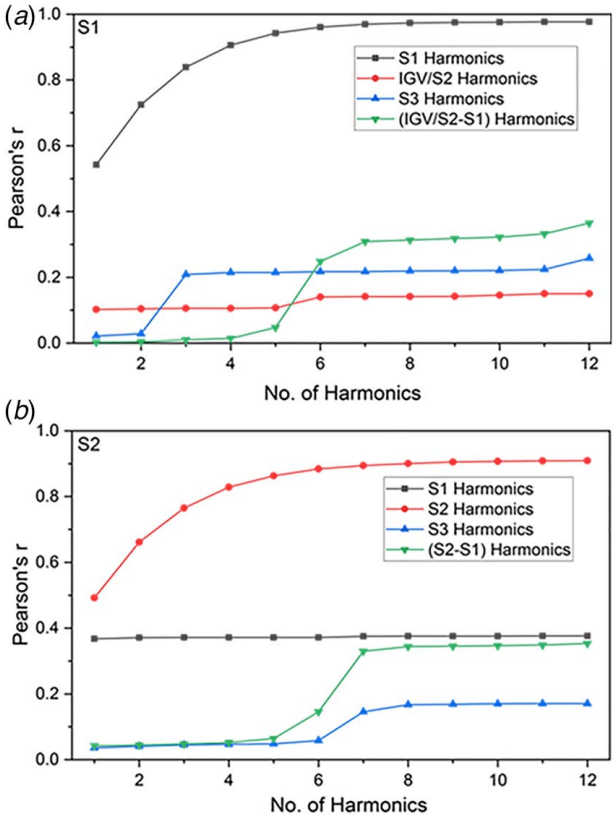

Fig. 11 Importance of the number of harmonics for reconstructing (*a*) stator 1 and (*b*) stator 2 total pressure field

As to the second dominant wavelet associated with the S1 wakes, there is a little increase in the reconstructed signal's confidence with the inclusion of additional harmonics. Therefore, one or two wavelets associated with the S1 wake are adequate. Lastly, to account for the influences of the S3 potential (50) and S1–S2 difference (6), the inclusion of only the fundamental wavelet associated with each mechanism is adequate. Following the same criteria, the appropriate number of harmonics to reconstruct the total pressure field downstream of S1 is obtained, and they are as follows:

(1) The first eight wavelets associated with S1 wake;
(2) The first two wavelets for IGV wake;
(3) The fundamental wavelet for S3 potential field;
(4) The fundamental wavelet regarding the 6/rev vane count difference effect.

5.4 Comparison of the Reconstructed Stator Exit Total Pressure With Experiment in Spatial Domain. With the dominant mechanisms and associated wavelets established, the total pressure downstream of stator 1 and stator 2 at midspan is reconstructed and compared with the experimental data, as shown in Fig. 12. The filled bands on the abscissa indicate the segments of data used for flow reconstruction. To illustrate the dominant influences on the circumferential flow nonuniformity in the total pressure field downstream of the S1 and S2, the signal is reconstructed using only the most dominant family of wavelets. By using the case of the reconstructed total pressure profile downstream of S1 as an example, as shown in Fig. 12(*a*), the reconstructed signal with the inclusion of only the wavelets associated with S1 wakes can characterize the 38/rev wake pattern nicely. However, there is no passage-to-passage variation in the reconstructed signal. Results from single-passage CFD simulations or experimental traverses fall in this category.

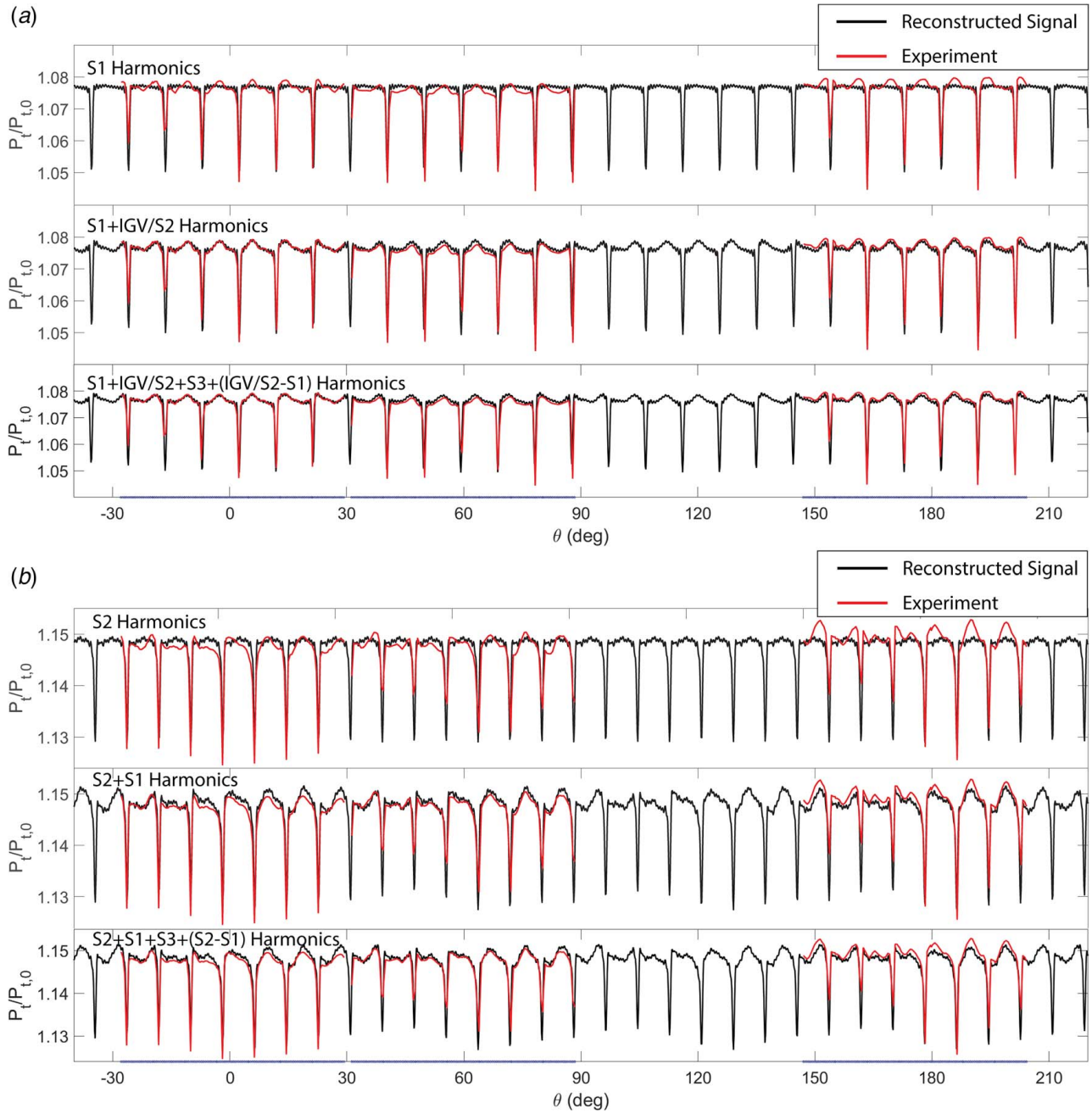

Fig. 12 Comparison of the reconstructed total pressure at midspan downstream of (*a*) stator 1 and (*b*) stator 2 with results from the experiment

Furthermore, there is a significant improvement in the agreement between the reconstructed signal and experimental data after taking the wavelets associated with IGV wakes into consideration. The reconstructed signal resolves the circumferentially nonuniform flow features very well, including wake and profile variability. This agreement between the reconstructed signal and experiment is reflected by the confidence of the reconstructed signal. The value of Pearson's r for the reconstructed signal reaches 98.1% after including the wavelets associated with IGV wakes. Lastly, there is a negligible change in the reconstructed signal after including wavelets associated with the potential field of S3 and the 6/rev pattern, which is expected according to the analysis in the previous section. The same conclusions also apply to the reconstruction of the total pressure field downstream of S2. The reconstructed signal with the inclusion of wavelets associated with S2 and S1 wakes can resolve the circumferentially nonuniform flow features very nicely with a confidence of 97.5%. There is little improvement in the reconstructed signal with the inclusion of the additional wavelets associated with the potential field of S3 and vane count difference.

Finally, there are some deviations between the reconstructed signal and experiment. For instance, the agreement between the reconstructed and experimental total pressure profiles downstream of S2 over the traverses at Location D is not as good as those acquired at Locations A and B. In addition, there are also deviations in predicting the wake depth for several passages. The first disagreement can be caused by rake hardware variations or geometric variations in seal clearances associated with imperfect rig concentricity. The deviations in the wake depth are likely caused by undersampling the experiment since a 5% vane passage resolution was utilized for the traverse. The root cause for these deviations will be investigated in future research.

Table 1 Values of Pearson's *r* for the reconstructed signal at all spanwise locations

Span (%)	12	20	35	50	70	80	88
S1	93	92	97	95	97	98	98
S2	97	98	98	95	93	97	97

5.5 Reconstructed Full-Annulus Total Pressure Field Downstream of S1 and S2. In a similar manner, the total pressure profiles downstream of S1 and S2 at the other six spanwise locations are reconstructed using the multiwavelet approximation method. Though not presented in detail here, good agreement was achieved at all spanwise locations between the reconstructed signal and experimental data, with a minimum confidence of 92%

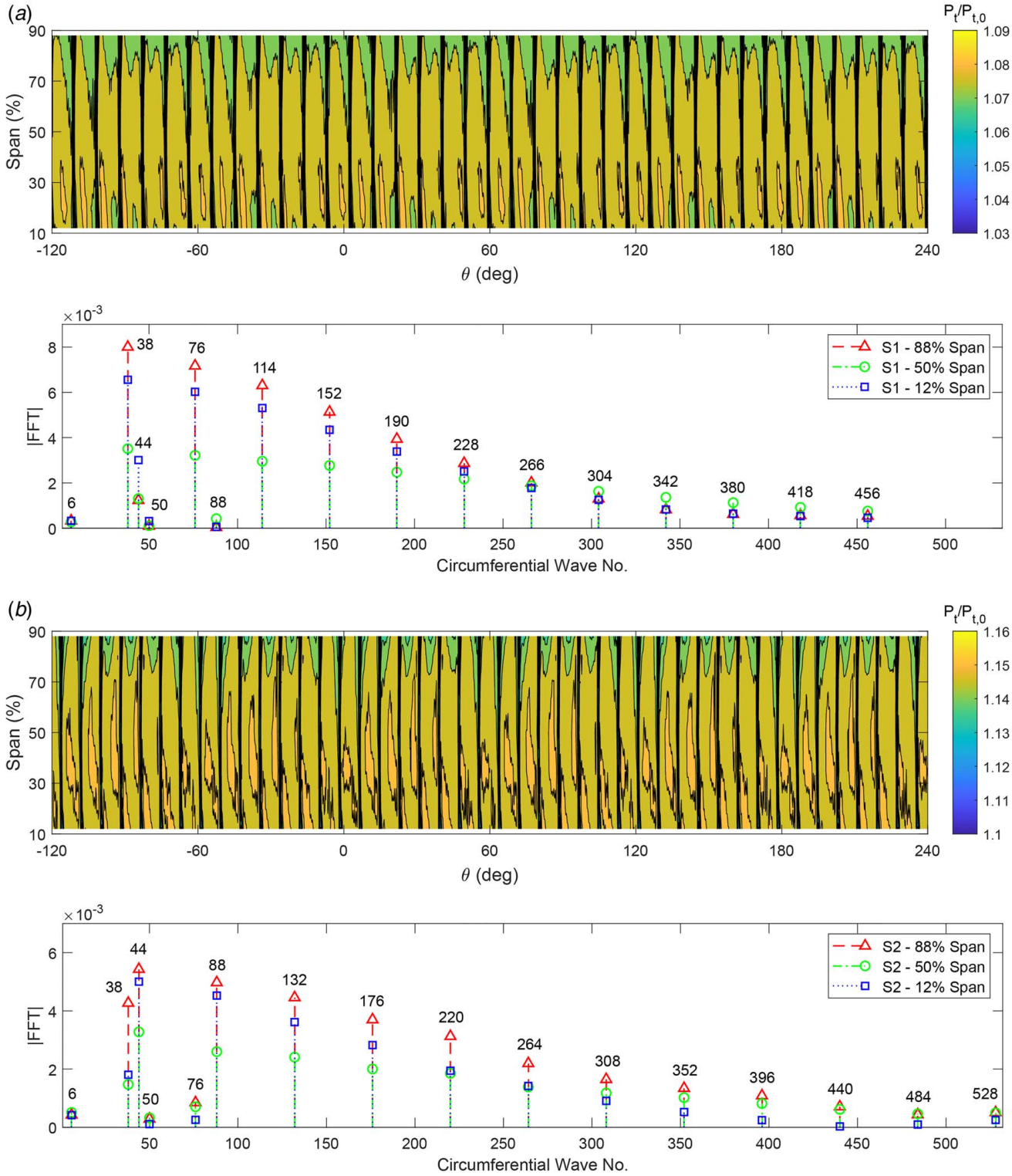

Fig. 13 Reconstructed total pressure field in both spatial and spectral domains for flow downstream of (*a*) stator 1 and (*b*) stator 2

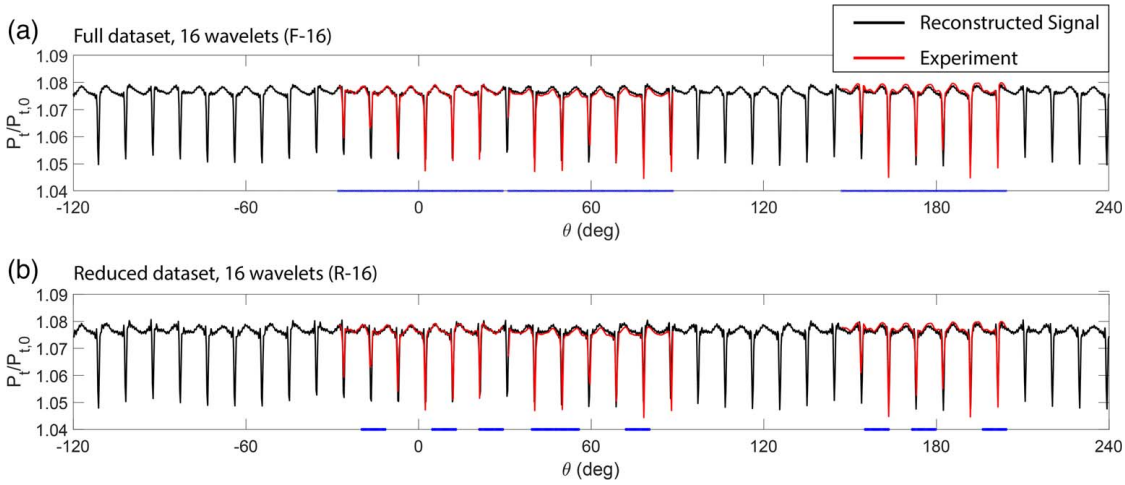

Fig. 14 Comparison of the reconstructed total pressure profiles downstream of s1 with experiment at 50% span from experiment using (*a*) full and (*b*) reduced dataset

in terms of Pearson's *r*, as listed in Table 1. With the reconstructed total pressure at all spanwise locations available, Fig. 13 shows the contour of the full-annulus total pressure field downstream of stator 1 and stator 2. The spectral magnitudes of the reconstructed total pressure at 12% (near hub), 50%, and 88% (near shroud) spanwise locations are also presented. In both cases, there are stronger aerodynamic excitations from flow near the end walls than at mid-span. For instance, in the total pressure field downstream of stator 1, the aerodynamic excitation magnitudes associated with the S1 wake at 88% and 12% spanwise locations are 87% and 128% higher than the value at midspan, respectively. The strongest aerodynamic excitation occurs near the blade tip. In addition, the wake–wake interaction gets intensified in the embedded stage, resulting in a stronger aerodynamic excitation associated with S1 wakes (38). For example, in the total pressure profile at 88% span downstream of stator 1, the magnitude of the aerodynamic excitation associated with IGV wakes (44) accounts for 15% of the value for the excitation related to S1 wakes (38). However, in the total pressure profile at 88% span downstream of Stator 2, the magnitude for the aerodynamic excitation associated with S1 wakes (38) reaches 79% of the excitation value related to S2 wakes (44).

5.6 Efforts Toward Reducing Input Data Size for Flow Reconstruction. The data used for flow reconstruction of the S2 exit flow field include measurements from 21 passages (7 traverses) with an approximate 48% coverage of the full-annulus, which is not a common luxury in real compressor or engine tests. To facilitate the implementation of the method, an effort was made to reconstruct the total pressure field using fewer data. To assure a high-fidelity result, an intelligent selection of the optimal traverse combinations included in the reduced dataset was exercised to achieve a small condition number. The condition number for reconstructing stator 1 downstream total pressure field is 2.16 (1.51 for full dataset) and is 2.77 (2.67 for full dataset) when reconstructing the total pressure field downstream of stator 2. The reduced dataset accounts for 43% of the full dataset and only 20% of the full-annulus coverage.

The reconstructed total pressure profiles at midspan downstream of S1 and S2 using the reduced dataset are shown in Figs. 14 and 15. Results from the experiment and the reconstructed signal using the full dataset are also shown in the figures. The segments of data used for flow reconstruction are indicated by the filled bands on the abscissa. In both cases, the reduced dataset yields good agreement in the total pressure profile between the reconstructed signal and experiment over the passages where experimental data were used for flow reconstruction. More importantly, good agreement is also achieved in the passages where the experimental data are not used for flow reconstruction. The features associated with passage-to-passage variations are nicely resolved in the reconstructed total

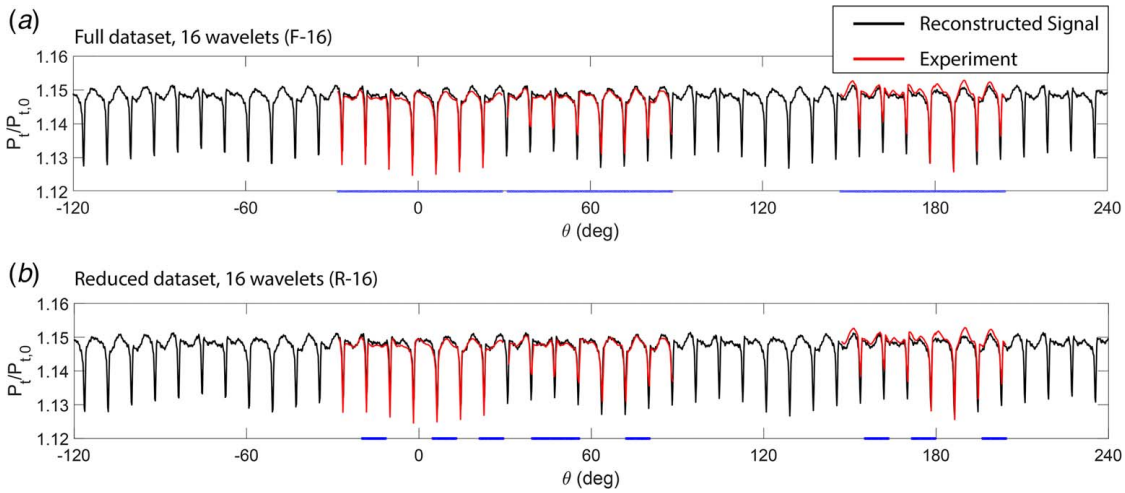

Fig. 15 Comparison of the reconstructed total pressure profiles downstream of s2 with experiment at 50% span from experiment using (*a*) full and (*b*) reduced dataset

Table 2 List of normalized mean total pressure at all spanwise locations

Span (%)	Stator 1		Deviation (%)	Stator 2		Deviation (%)
	F-16	R-16		F-16	R-16	
12	1.0740	1.0739	0.0059	1.1465	1.1464	0.0095
20	1.0755	1.0754	0.0134	1.1473	1.1472	0.0076
35	1.0766	1.0766	0.0083	1.1482	1.1481	0.0107
50	1.0752	1.0751	0.0068	1.1471	1.1470	0.0102
70	1.0739	1.0739	0.0008	1.1459	1.1457	0.0111
80	1.0714	1.0713	0.0037	1.1438	1.1437	0.0065
88	1.0691	1.0691	0.0006	1.1409	1.1408	0.0068

pressure profile using the reduced dataset. There are tiny differences between the two reconstructed total pressure profiles using the full and selected reduced datasets.

Lastly, the influence of data size on the mean total pressure obtained using the multiwavelet approximation method was investigated. Table 2 lists the normalized total pressure downstream of S1 and S2 using full datasets and reduced dataset. In both cases, the reduced dataset yields almost identical values for the mean total pressure at all spanwise locations, with a maximum deviation of less than 0.02%. This suggests that the circumferential flow nonuniformity in the stator exit total pressure field can be reconstructed from the reduced data set at high fidelity.

6 Conclusions

This article documents an effort to account for the circumferential flow nonuniformity associated with blade row interactions in the total pressure field downstream of the stators in a multistage axial compressor using a novel multiwavelet approximation method. The followings are a few important takeaways.

(1) In a multistage compressor with different vane counts, stator–stator interactions (including wake–wake interactions and wake–potential field interactions) result in nonuniform flow distributions around the annulus.
(2) This circumferentially nonuniform flow results in significant passage-to-passage variations, suggesting an aperiodic boundary condition among passages.
(3) Accounting for this circumferential flow nonuniformity is of great importance since measurements from discrete stationary instrumentation can be skewed in representing the true flow field. For instance, in the present study, the circumferential nonuniformity in total pressure alone can introduce an approximate 2.4-point variation in the calculated stage isentropic efficiency and a 54% variation in the spectral magnitudes of the aerodynamic excitation.
(4) The dominant mechanism influencing the circumferential nonuniformity in the total pressure field downstream of stators is the wake–wake interactions from the upstream vane row.
(5) The circumferentially nonuniform flow can be reconstructed from a small segment of data using a novel multiwavelet approximation method.
(6) The features associated with wake–wake interactions accounting for passage-to-passage variations are resolved in the reconstructed total pressure profile, yielding suitable mean flow performance properties and aerodynamic forcing functions.

Through the study, the multiwavelet approximation method shows excellent potential in accounting for the circumferential flow nonuniformity in multistage compressors. Lastly, though not presented here for brevity, the method has been successfully applied to different loading conditions as well as a variety of turbomachines, including both centrifugal and axial compressors [16].

Conflict of Interest

There are no conflicts of interest.

Data Availability Statement

The datasets generated and supporting the findings of this article are obtainable from the corresponding author upon reasonable request.

Nomenclature

h = enthalpy
k = condition number
$\boldsymbol{x}$ = vector of measurements
A = magnitude
N = number of wavelets
P = pressure
$\boldsymbol{A}$ = design matrix
$\boldsymbol{F}$ = vector of unknown coefficients
W_n = wavenumber
θ = circumferential positions of the measurements
π = total–total pressure ratio, $\pi = P_{t2}/P_{t1}$
ρ = Pearson's coefficient
φ = phase

Subscripts

AA = area average
exit = exit
i = the ith property
inlet = inlet
s = isentropic
t = stagnation properties

References

[1] Stoll, F., Tremback, J. W., and Arnaiz, H. H., 1979, "Effect of Number of Probes and Their Orientation on the Calculation of Several Compressor Face Distortion Descriptors," Technical Report, NASA Technical Memorandum 72859, National Aeronautics and Space Administration, Washington, DC.
[2] Stummann, S., Jeschke, P., and Metzler, T., 2015, "Circumferentially Non-Uniform Flow in the Rear Stage of a Multistage Compressor," ASME Turbo Expo 2015: Turbine Technical Conference and Exposition, Montreal, Quebec, Canada, June 15–19, ASME Paper No. GT2015-42935.
[3] He, L., Chen, T., Wells, R. G., Li, Y. S., and Ning, W., 2002, "Analysis of Rotor-Rotor and Stator-Stator Interferences in Multi-Stage Turbomachines," ASME J. Turbomach., **124**(4), pp. 564–571.
[4] Methel, J., Smith, N. R., Berdanier, R. A., and Key, N. L., 2018, "Effects of Circumferential Nonuniformity in Compressor Flow Fields Including Vane Wake Variability," J. Propul. Power, **34**(4), pp. 1080–1089.
[5] Chilla, M., Pullan, G., and Gallimore, S., 2020, "Reducing Instrumentation Errors Caused by Circumferential Flow Field Variation in Multistage Axial Compressors," ASME J. Turbomach., **142**(9), p. 091006.
[6] Besem, F. M., Kielb, R. E., Galpin, P., Zori, L., and Key, N. L., 2016, "Mistuned Forced Response Predictions of an Embedded Rotor in a Multistage Compressor," ASME J. Turbomach., **138**(6), p. 061003.
[7] Li, J., Aye-Addo, N., Kielb, R., and Key, N., 2018, "Mistuned Higher-Order Mode Forced Response of an Embedded Compressor Rotor—Part II: Mistuned Forced Response Prediction," ASME J. Turbomach., **140**(3), p. 031006.
[8] Li, J., Aye-Addo, N., Kormanik III, N., Matthews, D., Key, N., and Kielb, R., 2017, "Mistuned Higher-Order Mode Forced Response of an Embedded Compressor Rotor: Part I—Steady and Unsteady Aerodynamics," ASME Turbo Expo 2017: Turbine Technical Conference and Exposition, Charlotte, NC, June 26–30, ASME Paper No. GT2017-64633.
[9] Schoenenborn, H., 2018, "Analysis of the Effect of Multirow and Multipassage Aerodynamic Interaction on the Forced Response Variation in a Compressor Configuration—Part I: Aerodynamic Excitation," ASME J. Turbomach., **140**(5), p. 051004.
[10] Kormanik, N. J., Matthews, D. R., Key, N. L., and King, A. J., 2019, "Purdue 3-Stage Axial Compressor Research Facility: Through the Years, to Infinity,

and Beyond," AIAA Propulsion and Energy 2019 Forum, Indianapolis, IN, Aug. 19–22, p. 4000.
[11] Monk, D., 2014, "A Computational Analysis of the Aerodynamic and Aeromechanical Behavior of the Purdue Multistage Compressor," M.S. thesis, Mechanical Engineering, Purdue University, West Lafayette, IN.
[12] Kormanik N. J., III, 2017, "Characterization of Aerodynamic Forcing Functions for Embedded Rotor Resonant Response in a Multistage Compressor," M.S. thesis, Mechanical Engineering, Purdue University, West Lafayette, IN.
[13] Lemmon, E. W., Huber, M. L., and McLinden, M. O., 2013, "NIST Standard Reference Database 23: Reference Fluid Thermodynamic and Transport Properties-REFPROP," Version 9.1, National Institute of Standards and Technology, Standard Reference Data Program, Gaithersburg, MD.
[14] Lou, F., Fabian, J. C., and Key, N. L., 2013, "The Effect of Gas Models on Compressor Efficiency Including Uncertainty," ASME J. Eng. Gas Turb. Power, **36**(1), p. 012601.
[15] Lou, F., and Key, N. L., 2021, "Reconstructing Compressor Non-Uniform Circumferential Flow Field From Spatially Undersampled Data—Part 1: Methodology and Sensitivity Analysis," ASME J. Turbomach., **143**(8), p. 081002.
[16] Lou, F., Matthews, D. R., Kormanik, N. J., and Key, N. L., 2021, "Reconstructing Compressor Non-Uniform Circumferential Flow Field From Spatially Undersampled Data—Part 2: Practical Application for Experiments," ASME J. Turbomach., **143**(8), p. 081003.